CALCULATION OF THE SEISMIC IMAGING COMPLEXITY OF COMPLEX GEOLOGICAL STRUCTURES

GAOXIANG CHEN[1], LI-YUN FU[1], KAN FU CHEN[2], WEIJIA SUN[1], WEI WEI[1] and XIZHU GUAN[1]

[1] *Institute of Geology and Geophysics, Chinese Academic of Science, Beijing 100029, P.R. China. hncschengaoxiang@126.com; lfu@mail.iggcas.ac.cn*
[2] *Zhejiang Provincial Institute of Communication, Planning, Design and Research, Zhejiang 310000, P.R. China.*

(Received May 4, 2016; revised version accepted December 15, 2016)

ABSTRACT

Chen, G., Fu, L.-Y., Chen, K.F., Sun, W., Wei, W. and Guan, X., 2017. Calculation of the seismic imaging complexity of complex geological structures. *Journal of Seismic Exploration*, 26: 81-104.

Quantitative analysis of geological complexity in terms of seismic imaging is an important way to measure the coherent interaction of geological heterogeneity spectra with the migrator used. Based on previous studies, we introduce several new strategies to evaluate the complexity of subsurface heterogeneous media, the main features of which are use of a velocity co-occurrence matrix for velocity variations and use of the Hough transform for dip-angle calculations. First, the velocity co-occurrence matrix is created by statistically classifying adjacent-point velocity contrasts, after which the scaling characteristics of migrators are directly incorporated into the matrix for presenting seismic imaging complexity. Second, vertical velocity variations are also taken into account using a depth-velocity co-occurrence matrix. Third, we apply the high-precision Hough transform to locate geological interfaces and estimate the dip angle of each point before calculating angular complexity. Finally, considering the indivisibility of the effect of both lateral/vertical velocity variations and dip angles, we define a comprehensive coefficient to assess the seismic imaging complexity of complex geological structures. Tests on the 2D SEG slat model and field data demonstrate that the new strategies proposed for evaluating geological complexity are reliable and applicable to different degrees of geological complexity due to the sensitivity of the method for detecting small and large velocity contrasts as well as dip-angle variations.

KEY WORDS: velocity co-occurrence matrix, Hough transform, geological complexity, relative error function, seismic imaging.

0963-0651/17/$5.00

INTRODUCTION

The majority of hydrocarbon-bearing formations in China are located in the northwestern basins and eastern plains. After multiple stages of tectonic activity, the northwestern compressional basins display extremely complex geological structures, such as steeply dipping reverse thrusts; salt-pierced conformations; and high, steep faults. In contrast, in the eastern plains, the subsurface structures are mainly dominated by numerous tensile fracture belts comprising tilted faults and torsional deformation. All these complex structures are challenging for seismic imaging because of their strong lateral heterogeneity and dip angles. The interactions of imaging wavefields with heterogeneous slabs in seismic migration has been addressed in several geophysical studies: imaging accuracy, velocity variations, and dip angles are closely correlated at various scales. Quantitative evaluation of geological complexity as well as seismic imaging complexity is important for optimizing seismic data acquisition; improving seismic processing and interpretation; and, in particular, selecting an optimal migration method for a given seismic dataset to achieve the best compromise between imaging quality and computational efficiency.

Over the past few decades, numerous migration methods have been developed to image complex structures with varying degrees of complexity at different computational costs. There are various methods available for data processing, many of which may be more than adequate to the task. There is no quantifiable criterion to guide the choice of methods in terms of geological complexity. For a given seismic dataset, the ideal migration method should exactly fit the geological complexity to ensure imaging accuracy at a minimal computational cost. Geological complexity is a relative concept in seismic migrators, i.e., a complex geological structure presents different complexities to different seismic migrators. To quantitatively assess this type of seismic imaging complexity, correlating the scaling characteristics of heterogeneities (in both lateral velocity variations and dip angles) with those of migrators is necessary. Fu (2010) proposed a tentative strategy for quantitative evaluation of the complexity of subsurface heterogeneous media to determine which scales of geological heterogeneities are captured by waves. In this strategy, geological heterogeneities are expressed as the slowness- and angular-heterogeneity spectra to quantify the velocity contrasts and dip-angle distributions of complex geological structures, respectively. On the other hand, the scaling characteristics of a propagator are measured through dispersion analysis by its angular spectra plotted against refractive indexes and propagation angles. Finally, a parameter, which is termed the complexity coefficient, is defined by associating the geological heterogeneity spectra with the propagator's angular spectra to understand the coherent interference between the heterogeneity of the medium and the scaling characteristics of the propagator. This strategy provides a means of quantitative analysis of geological complexity in terms of seismic propagators. From application to Kuqa field data (Dong et al., 2011; Fu et al.,

2013), the method appears to be reliable in most cases, except in some special situations due to its inherent defects in the following aspects: (1) the slowness-heterogeneity spectrum expressed as a velocity probability density cannot reflect lateral velocity variations exactly; (2) the method takes no account of vertical velocity variations that may complicate wave propagation, particularly in the presence of a high-to-low velocity reverse; and (3) the angular-heterogeneity spectrum obtained by a simple windowed scanning algorithm cannot achieve an accurate dip-angle distribution when geological interfaces in seismic profiles are characterized by low continuity, a high degree of curvature, or significant cross bedding.

In this article, the strategy is extended to seismic imaging. Particular attention is paid to overcoming the limitations mentioned above by means of several algorithms. First, a velocity co-occurrence matrix (VCM) is used to highlight velocity variations by statistically classifying adjacent-point velocity contrasts. The matrix can detect subtle velocity variations through careful choice of the maximal contrast. Furthermore, the scaling characteristics of migrators are directly incorporated into the matrix for the presentation of seismic imaging complexity. Second, vertical velocity variations are taken into account. Third, we introduce the Hough transform to improve the dip-angle calculation, by which both the position and angle of each point along an interface can be precisely detected. Finally, as the effect of both lateral/vertical velocity variations and dip angles cannot be separated for assessment in the seismic imaging procedure, we introduce a comprehensive coefficient to assess the seismic imaging complexity of complex geological structures. Some numerical examples with salt-pierced structures and complex faults are used to illustrate the applicability and performance of these techniques.

ANALYSIS OF SEISMIC IMAGING COMPLEXITY

Angular spectra of seismic migrators

With the requirement of accuracy in seismic imaging, an increasing number of migration methods have been developed to image steep dips under strong velocity contrasts. In general, a wave-equation-based migrator has an analytical dispersion equation to quantify its accuracy. It is possible to calculate the analytical dispersion equation using an angular spectrum in which the imaging accuracy is displayed as functions of velocity perturbation and propagation angle. In this article, we take Fourier-transform-based methods as examples for dispersion analyses due to their many desirable properties, such as analytical wavefield extrapolation, algorithm simplicity, high computational efficiency, amplitude preservation by honoring Snell's law naturally, and immunization against both grid dispersion and operator splitting errors occurring in 3D cases (Fu, 2005).

After the phase-shift migrator (Gazdag, 1978) for laterally homogeneous slabs, several typical Fourier migrators for wavefield extrapolation have been designed for lateral velocity variations by approximating the square root equation with different accuracies and computational costs, such as the split-step Fourier (SSF; Stoffa et al., 1990) or phase-screen migrator (Wu, 1996) for either weak-contrast slabs or small propagation angles; the pseudoscreen (Wu, 1996; Huang et al., 1999) and generalized screen migrators (de Hoop et al., 2000; Le Rousseau and de Hoop, 2001) for large-contrast slabs; the high-order separation-of-variables screen migrators (Fu and Duan, 2002; Fu, 2006); and the Fourier finite-difference migrator (FFD; Ristow and Rühl, 1994) for strong-contrast slabs. Let $u(k_x,z)$ denote the 2D time-harmonic scalar wavefield in the frequency-wavenumber domain, where k_x is the wavenumber with respect to x and z is the depth. For wavefield extrapolation through a laterally heterogeneous slab Δz, these Fourier migrators can be generally expressed as $u(k_x,z + \Delta z) = \hat{u}(k_x,z)\exp(ik_z\Delta)$, where $k_x^2 + k_z^2 = k_0^2$ and the wavenumber $k_0 = \omega/v_0$ with the constant reference velocity v_0 for the slab. In Fourier migration techniques, two steps are involved in wavefield extrapolation: the phase shift in the wavenumber domain by a reference velocity and the phase-screen interaction (plus an extra finite difference (FD) implementation for the FFD) in the space domain. The procedure is repeated for each frequency and each slab. A fast Fourier transformation is frequently used to shuttle wavefields between these two domains.

The intermediate wavefield $\hat{u}(k_x,z)$ can be obtained by different Fourier migrators for different accuracies. For instance, the SSF method takes $\hat{u}(k_x,z) = FT_x[u(x,z)\exp\{ik_0\Delta z(n(x)-1)\}]$ with the dispersion equation

$$\bar{k}_x^2 + [\bar{k}_z-(n-1)]^2 = 1 \quad ,$$

where FT_x is the forward Fourier transform ($x \rightarrow k_x$) and n(x) the refractive index.

For the FFD, the corresponding dispersion equation can be rewritten as

$$\bar{k}_z = \sqrt{(1-\bar{k}_x^2)} + n - 1 + \sum_{i=1}^{m} \{a_j(n)\bar{k}_x^2/[1 + b_j(n)\bar{k}_x^2]\} \quad , \qquad (1)$$

where a_j and b_j functions of n changing with lateral velocity variations. The third item on the right-hand side of eq. (2) is called the parabolic correction term, which is incorporated to handle strong lateral velocity variations. The cross-coupling of k_z and n in this term indicates that eq. (1) is not a separation-of-variables operator expression and consequently requires an extra implicit FD implementation.

Based on these dispersion equations, it is possible to measure the imaging accuracy as functions of lateral velocity variation and propagation angle. The relative phase error for imaging accuracy can be defined as $e = \delta\varphi - 1$, where $\delta\varphi$ is the phase perturbation. Using the dispersion equations, the correlation of the propagation angle θ, the refractive index n, and the imaging accuracy e can be explicitly expressed as an angular spectrum of the cross-plot of propagation angles and refractive indexes. For instance, the SSF and FFD migrators correspond to the following respective angular spectra:

$$e_{SSF} = p(n,\theta)_{SSF} = |n\sqrt{(1-\sin^2\theta)} - \sqrt{(1-n^2\sin^2\theta)} + (1-n)| \\ /n\sqrt{(1-\sin^2\theta)} \quad , \tag{2}$$

$$e_{FFD} = p(n,\theta)_{FFD} = |n\sqrt{(1-\sin^2\theta)} - \sqrt{(1-n^2\sin^2\theta)} + (1-n) + n(1-n) \\ \times \{\sin^2\theta/[2-0.5(n^2+n+1)\sin^2\theta]\}| \; / \; n\sqrt{(1-\sin^2\theta)} \quad , \tag{3}$$

It is apparent that the parameters θ and n in the angular spectra act as a bridge between imaging accuracy and geological heterogeneity. For a given imaging accuracy e, efficient seismic imaging requires the migrator's angular spectrum to provide a band-pass filter defined by θ and n for dominant heterogeneous components in the slab. This provides a possible way to assess geological complexity in terms of seismic migrators.

Slowness-heterogeneity spectrum from a lateral/vertical velocity co-occurrence matrix

Velocity variations in a slab can be measured in terms of two quantities: the proportion of each velocity in the whole slab and the contrast between velocity components. In contrast to the former, the latter increases the complexity of velocity variations in seismic imaging. Both the quantities should be properly taken into account for the slowness-heterogeneity spectrum of velocity variations. Lateral velocity variations are often treated as the main factor affecting seismic imaging; however, little attention has been paid to vertical velocity variations in seismic imaging. Complex geological structures, such as penetrating salts and salt-related overthrusts, often cause vertical velocity turnovers, significantly attenuating upward waves from complex subsalt zones. In this article, we regard these salt-related and irregular high-velocity layers as another factor that affects seismic imaging.

As mentioned in the introduction, Fig. 1 illustrates the inability of the traditional slowness-heterogeneity spectrum (Fu, 2010; Dong et al., 2011; Fu et al., 2013) to measure the lateral distribution of velocities exactly. Figs. 1a-1c show three slabs constructed from the same velocity components but with

different geological structures. Despite the obvious differences in velocity distribution, these slabs share the same velocity probability density, as shown in Fig. 1d. The velocity probability density is obtained by counting the number of points with the same velocity value in a slab, but without considering their spatial arrangement. The slowness-heterogeneity spectrum expressed as a velocity probability density cannot differentiate velocity structures.

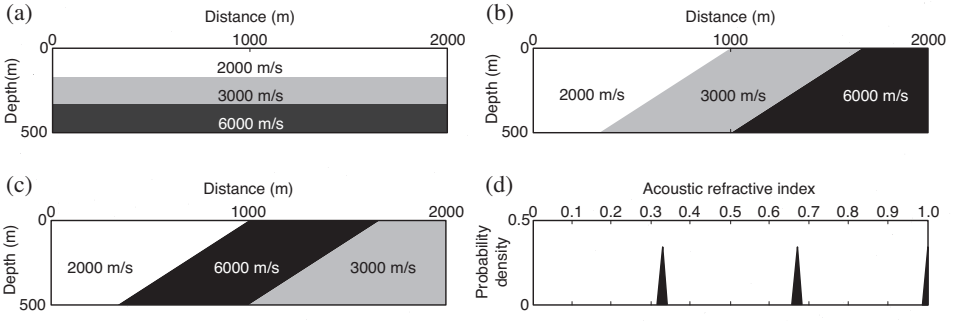

Fig. 1. Three different velocity models (a), (b), and (c) that share the same velocity probability density (d).

To avoid this defect in velocity probability density, we introduce the gray level co-occurrence matrix (GLCM; Haralick et al., 1973) used in the texture analysis of images to describe spatial variations in a velocity distribution. The GLCM is a measure of how often different combinations of neighboring pixel values occur in an image. The GLCM method has been widely applied in seismic amplitude texture analyses (Gao, 2003; Chopra and Marfurt, 2005; Gao, 2007; Yenugu et al., 2010; Eichkitz et al., 2015) for seismic image visualization and facies classification. The method extracts textural features in a seismic image via a co-occurrence matrix depicting spatial relations or patterns of neighboring amplitudes. Similarly, the spatial variability in the velocity components of a slab can be evaluated at each sample location by means of a velocity co-occurrence matrix.

Fig. 2a presents a 2D velocity distribution ranging from v_{min} to v_{max}, in which two arbitrary points (i,j) and (i+n,j+n) with velocities and $v_{i,j}$ and $v_{i+n,j+m}$ (i,n = 1,2,...,N_x; j,m = 1,2,...,N_z), respectively, can be connected by dip steering with a straight line L and an angle α with respect to the x-axis. We can set a velocity pair $(v_{i,j},v_{i+n,j+m})$ for the velocity contrast between these two locations. By changing L and α, theoretically a total of $0.5 \times (N_x \times N_z) \times (N_x \times N_z - 1)$ velocity pairs can be obtained. With dip steering, it is possible to control the direction for co-occurrence matrix computations to describe the spatial variations of velocity in different directions. Considering lateral/vertical velocity variations for seismic imaging, we simply choose $\alpha = 0°/90°$ and $L = \Delta x/\Delta z$, resulting in lateral/vertical VCMs.

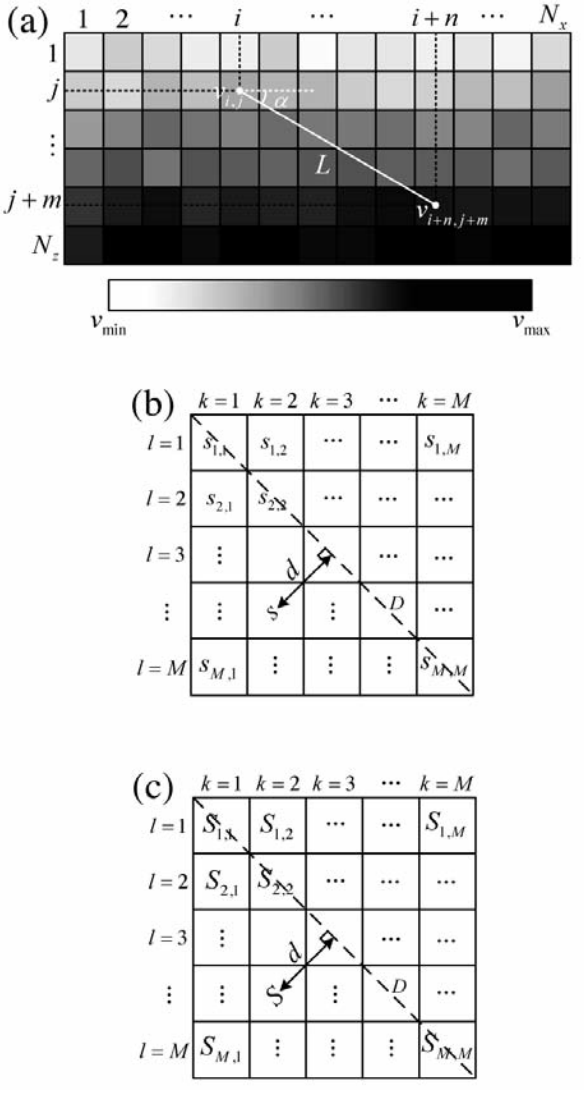

Fig. 2. Schematic diagram of velocity co-occurrence matrix computation. (a) A 2D velocity distribution ranging from v_{min} to v_{max}, in which two arbitrary points (i,j) and (i+n,j+m) create a velocity pair ($v_{i,j}$,$v_{i+n,j+m}$). (b) The lateral and (c) the vertical velocity co-occurrence matrixes for the velocity model in Fig. 2a.

For convenience in calculating co-occurrence matrixes, we normalize each velocity value $v_{i,j}$ into an integer $V_{i,j}$ within the range 1−M (M is the order of the VCM) using the equation

$$V_{i,j} = round\{[(v_{i,j} - v_{min})/(v_{max} - v_{min})](M-1) + 1\} \quad , \tag{4}$$

where *round*() rounds each element to the nearest positive integer. From the modified velocity model, we compute each element $s_{k,l}$ of a VCM of size M×M using the equation

$$s_{k,l} = \sum_{i=1}^{N_x} \sum_{j=1}^{N_z} (V_{i,j} = k,\ V_{i+n,j+m} = l) \quad , \tag{5}$$

where k,l = 1,2,...,M. The resulting lateral/vertical VCMs are shown in Figs. 2b and 2c, respectively, in which $s_{k,l}$ (or $S_{k,l}$ for the vertical VCM) denotes the number of occurrences (counts) of adjacent points with the same velocity pair $(v_{i,j},v_{i+n,j+m})$ in a specific direction defined by L and α. Rather than the velocity probability density, these lateral/vertical VCMs characterize spatial variability across all velocity components, both considering their contrasts and depicting their spatial relations to or the patterns (i.e.,., structures) of neighboring components.

Before conducting analyses of velocity variations, the lateral/vertical VCMs should be optimized to improve their applicability to models of different sizes and varying velocity variations. It is worth mentioning that the VCMs are more than just a counter, as the indexes l and k are relevant to real velocities with a contrast proportional to the distance d = $|l - k|/M$ from an arbitrary position s (or S) to the leading diagonal D, as illustrated in Figs. 2b and 2c. The elements in the bottom-left and top-right corners have the largest velocity contrasts, and the leading diagonal denotes elements without velocity perturbations. We use d^2 as a scaling coefficient to optimize each element of the VCMs at an exponential rate to differentiate each from others located in different positions. For analytical convenience, we normalize each VCM by dividing it by the sum of all its elements to make the results independent of the size of the velocity model.

Fig. 3 shows the lateral (Figs. 3a-3c) and vertical (Figs. 3d-3f) VCMs for the three different velocity models in Fig. 1, where M = 10 and the small squares indicate nonzero elements with varying gray levels. For quantitative comparison of different elements, these squares are marked with their accurate values as well as their velocity pairs. The three black squares along the leading diagonal of each VCM represent the domain with the same velocity component. The absence of nonzero elements, except for the leading diagonal in Fig. 3a, exactly corresponds to the constant lateral velocity distribution in Fig. 1a. The gray squares in Figs. 3b and 3c indicate lateral velocity variations between one domain and its adjacent neighborhood in the horizontal direction, as illustrated in Figs. 1b and 1c. In addition, the locations of these gray squares denote different velocity pairs; similarly, the gray squares in Figs. 3d-3f indicate vertical velocity variations.

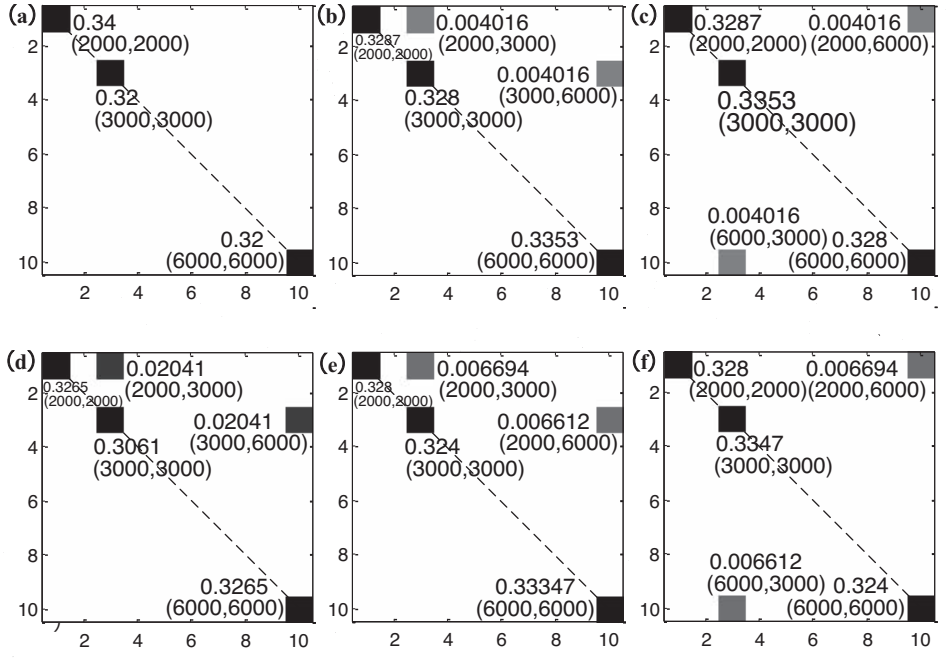

Fig. 3. Lateral [(a)-(c)] and vertical [(d)-(f)] VCMs for the respective velocity models illustrated in Figs. 1a-1c.

Interaction between lateral/vertical VCMs and seismic migrators

The revised VCMs take into account both velocity compositions and lateral/vertical variations. Incorporation of seismic migrators into the lateral/vertical VCMs is key to quantifying seismic imaging. In general, different migrators have different localization features: none of the migrators can globally account for all of the velocity contrasts and dip angles. To obtain optimum seismic imaging, we expect that the spectrum of a given migrator will coincide with the heterogeneity spectra of the slab, expressed as the lateral/vertical VCMs.

Direct incorporation of the angular spectrum of a seismic migrator into the VCMs is convenient for the presentation of seismic imaging complexity with respect to lateral/vertical velocity variations. Based on eqs. (2) and (3), the angular spectra $g(n,e) = \theta$ of the SSF and FFD migrators can be numerically calculated for a given phase error, for example, $e = 10\%$. To incorporate the angular spectra into the VCMs, we first revise the angular spectra as $q = 1 - g'(n,e)$ with $g'(n,e)$ denoting the normalization of $g(n,e)$. The resulting spectra are shown in Fig. 4a, in which the normalized angular error curves are

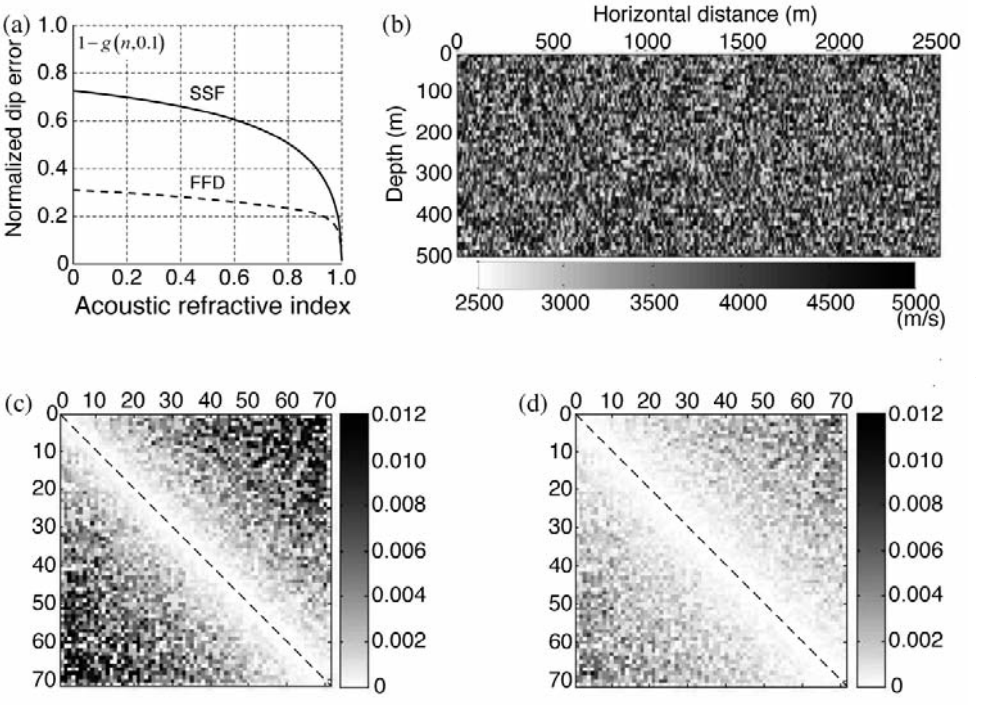

Fig. 3. Lateral [(a)-(c)] and vertical [(d)-(f)] VCMs for the respective velocity models illustrated in Figs. 1a-1c.

Interaction between lateral/vertical VCMs and seismic migrators

The revised VCMs take into account both velocity compositions and lateral/vertical variations. Incorporation of seismic migrators into the lateral/vertical VCMs is key to quantifying seismic imaging. In general, different migrators have different localization features: none of the migrators can globally account for all of the velocity contrasts and dip angles. To obtain optimum seismic imaging, we expect that the spectrum of a given migrator will coincide with the heterogeneity spectra of the slab, expressed as the lateral/vertical VCMs.

Direct incorporation of the angular spectrum of a seismic migrator into the VCMs is convenient for the presentation of seismic imaging complexity with respect to lateral/vertical velocity variations. Based on eqs. (2) and (3), the angular spectra g(n,e) = θ of the SSF and FFD migrators can be numerically calculated for a given phase error, for example,e = 10%. To incorporate the angular spectra into the VCMs, we first revise the angular spectra as q = 1−g′(n,e) with g′(n,e) denoting the normalization of g(n,e). The resulting spectra are shown in Fig. 4a, in which the normalized angular error curves are

The MVCMs take into account both lateral/vertical variations and migrator characteristics, by which it is possible to define a scalar coefficient to measure the complexity of geological models for seismic imaging. As mentioned previously, the GLCM is well known for its potential in terms of distinguishing different textural features of a normal image by a scalar coefficient acquired from different definitions, such as angular second moment, contrast, and correlation. Similarly, a complexity coefficient can be defined from the MVCMs in the same way. Of the several textural features of the MVCMs, we choose the following expression as the definition of the lateral complexity coefficient h_cmp,

$$\text{h\_cmp} = \sum_{k=1}^{M} \sum_{l=1}^{M} [(k-l)/M]^2\{1 - g'[\min(k,l)/\max(k,l),e]\}s_{k,l}^2 \quad . \tag{6}$$

A slight modification of eq. (6) yields the vertical complexity coefficient v_cmp,

$$\text{v\_cmp} = \sum_{k=1}^{M} \sum_{l=1}^{k} [(k-l)/M]^2\{1 - g'[\min(k,l)/\max(k,l),e]\}s_{k,l}^2 \quad . \tag{7}$$

For the vertical velocity complexity, we focus only on the location of velocity reversals along the depth direction. In fact, the VCMs automatically classify all the velocity pairs into three different regions: (1) the lower triangular region ($k < l$), in which the velocities are higher for the overlying strata than for the underlying strata; (2) the leading diagonal ($k = l$) for equal velocities; and (3) the upper triangular region ($k > l$), in which the velocities are smaller for the overlying strata than for the underlying strata. As indicated in eqs. (6) and (7), we only consider elements in the first region for the computation of complexity coefficients.

We use the models illustrated in Fig. 1 as examples to test the applicability of these complexity coefficients. It is obvious by intuition that the horizontally layered model in Fig. 1a shows no lateral velocity variations, whereas the model in Fig. 1c with a high-velocity dipping interlayer should be more complex than that in Fig. 1b. This type of high-velocity dipping interlayers or salt structures often cause strong lateral contrasts. We compute the lateral/vertical complexity coefficients of these models in terms of the SSF and FFD migrators. The results are listed in Table 1. The lateral complexity coefficients of the model in Fig. 1c are higher than those of the model in Fig. 1b for both migrators. The coefficients increase much more for the SSF than for the FFD migrators. Therefore, the geological complexity represented quantitatively by the lateral complexity coefficients listed in Table 1 agrees with the intuitive estimation for these models. For the vertical complexity coefficients, the zero values indicate no velocity inversion along the depth

direction for the models in Figs. 1a and 1b, whereas the vertical velocity turnover from 6000 m/s down to 3000 m/s for the model in Fig. 1c results in nonzero vertical complexity coefficients for the SSF and the FFD migrators.

Table 1. Lateral/vertical complexity coefficients of the three models illustrated in Fig. 1

	h_cmp			v_cmp	
model	SSF	FFD	model	SSF	FFD
(a)	0	0	(a)	0	0
(b)	0.24	0.10	(b)	0	0
(c)	0.45	0.19	(c)	0.37	0.16

Calculation of angular complexity based on the Hough transform

As one of the main descriptions of geological structures, dip angle is a key factor affecting seismic imaging. To quantify the dip-angle distribution in a geological structure, Fu (2010) proposed an angular-heterogeneity spectrum by calculating the angular probability density through edge detection, window scanning, and dip-angle estimation for each point in a velocity model or a seismic section. The reliability and accuracy of these techniques depend heavily on precisely how the geological interfaces are located and the angles are calculated. Conventional techniques for edge detection are mainly based on gradient operators, such as the Robert, Prewitt, Laplacian, and Kirsch operators (Bourgeois et al., 1991). These gradient operators for interface positioning, plus simple window scanning for angle estimation, work well for simple geological structures with noiseless images. However, for complex structures with noise-polluted images, these edge-detection and angle-estimation techniques give an unsatisfactory performance because of algorithmic defects such as window shape/size dependency; for instance, each point will be assigned an angular value no matter whether an interface is present or not. In this section, we attempt to improve the accuracy of edge detection and angle estimation by applying the Hough transform (Hough, 1959; Guil et al., 1995).

The classical Hough transform was originally created to identify straight lines in an image before being developed to detect arbitrary shapes, most commonly circles or ellipses. In the simplest case, an arbitrary straight line l at an angle θ to the x-axis can be expressed as

$$x\cos\theta + y\sin\theta = \rho \quad , \tag{8}$$

where ρ is the distance from the origin to the nearest point on l. Eq. (8) demonstrates that any straight line in the (x,y) space is associated with a unique parameter pair (θ,ρ), based on which the Hough transform is developed. Fig. 5 gives a simple description of how a straight line in an image is converted into a single point in the θ-ρ domain by the Hough transform. Fig. 5a is an input image, in which the black dots mark the potential straight lines; for instance, the dots falling on l_1 are treated as a real line and may be detected. In general, four main steps are needed to complete the transform: (1) determine the potential line in the image in terms of (x,y) coordinates using eq. (8) according to the given parameter (θ,ρ); (2) count the number of dots located on the line before storing the number in the bin of (θ,ρ) in Fig. 5b; (3) repeat the above two steps until each bin in the θ-ρ domain is completed; and (4) execute a global search of all the bins for values higher than a threshold that is set as a parameter to extract the points that are most likely to be located on straight lines. For instance, in the case of Fig. 5, if the threshold is set as 40, then bin B2 is abandoned while B1 is retained because the latter has a higher value than the threshold. As the coordinates of bin B1 are known, it is easy to locate the line that consists of 50 dots in Fig. 5a.

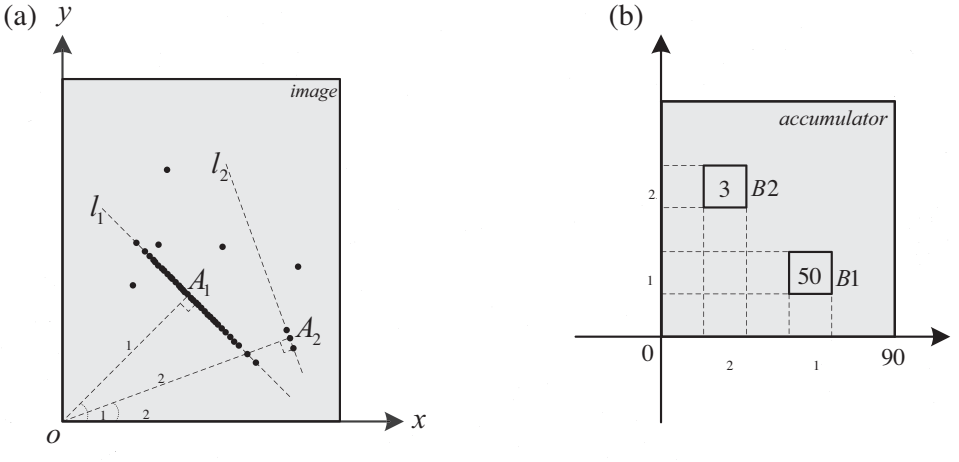

Fig. 5. Sketch of the method for transforming a single line (a) into a single point (b) using the Hough transform.

Regardless of the configuration of any random region of geological interfaces, the straight-line Hough transform still performs well if the input parameters are appropriately selected, because large-scale bent curves can be properly approximated by small-scale straight lines. This is demonstrated by the following experiment. Fig. 6a shows a black-and-white image containing many

geological interfaces resulting from applying an edge detector to a geological model with dip angles ranging from 0° to nearly 90°. The computed Hough space (θ,ρ) is displayed in Fig. 6b, in which the gray level represents the number of points located on the same line, depending on which the spatial distribution is recalculated with dip angles for all the interfaces shown in Fig. 6c. The profile in Fig. 6c perfectly restores the spatial distribution with dip angles for all the interfaces compared to Fig. 6a, without redundant information emerging in places with no interfaces. Furthermore, the gray levels provide a clear and readable dip-angle distribution for the whole model. This experiment demonstrates the applicability of the straight-line Hough transform in detecting irregular geological interfaces as well as in estimating dip angles.

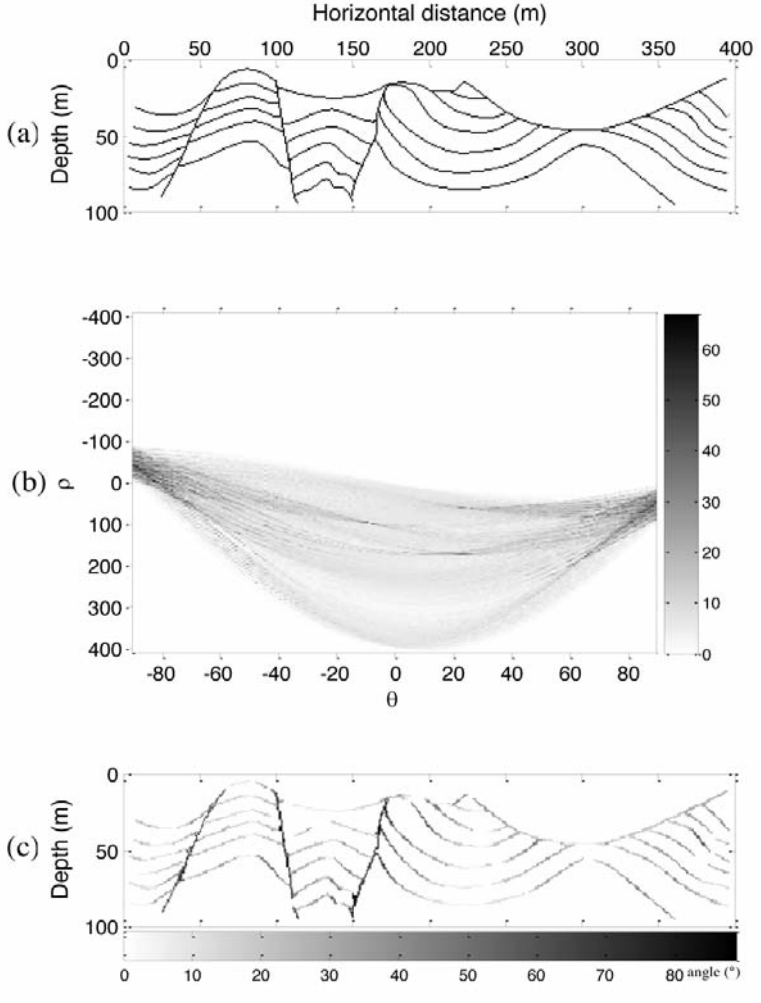

Fig. 6. A black-and-white image (a) with many geological interfaces, the corresponding Hough transform spectrum (b), and the restored spatial distribution (c) with dip angles.

Based on the dip-angle distribution obtained by the Hough transform (Fig. 6b), the angular probability density can be calculated for angles in the range 0°-90°, with an interval of $\Delta\theta = 1°$. The resulting angular-heterogeneity spectrum $q(\theta)$ is illustrated in Fig. 7a. Physical interpretation of the spectrum is not difficult. The probability density at each value of θ is the density of data points falling in the interval $\Delta\theta = 1°$ centered at θ. The spectrum shows a full span of dip angles in the model from 0° to 90°, with most angles being less than 50°. To measure the angular-localization feature of a migrator for complex models, it is necessary to look at the coherent interference between the angular-heterogeneity spectrum $q(\theta)$ of a geological model and the angular spectrum $p(n,\theta)$ of a migrator. As shown in Fig. 7b for the SSF and FFD migrators, the angular spectrum is plotted as a function of the propagation angle θ under a constant refractive index $n = 0.25$. Following Fu (2010), we define a coefficient *a*_cmp, termed the angular complexity coefficient, to quantify the performance of a migrator in imaging dipping strata for a given dataset

$$a\_\mathrm{cmp} = \int_{0°}^{90°} q(\theta)p(n,\theta)d\theta \quad . \tag{9}$$

For the example illustrated in Fig. 7, angular complexity coefficients of 0.24 and 0.06 are obtained for the SSF and FFD migrators, respectively. These angular complexity coefficients quantify the coherent interference of two types of spectra, in which the dominant components in the angular-heterogeneity spectrum of a complex model will be imaged efficiently and perfectly if they are situated in the illuminated area of the migrator's angular spectrum; conversely, for components in a "dark" area, poor imaging and strong noise will be expected.

CASE STUDIES

Based on separate analyses of velocity and angular variations in the previous sections, we apply the strategy to both the 2D SEG/EAGE salt model and the classical fault model in eastern China. We attempt to create a criterion for evaluating geological complexity in terms of seismic migrators. The problem is how to allocate the proportions of velocity and angular complexities in terms of their coupled relationship in seismic imaging. For simplicity, we sum both as a comprehensive complexity coefficient, assuming that the velocity and angular variations have the same effect on seismic imaging.

The salt model illustrated in Fig. 8a has strong velocity contrasts up to $n \approx 0.35$ and steep dips up to a maximum of 70°. There are several crucial targets to challenge seismic imaging methods, such as the strong-contrast salt

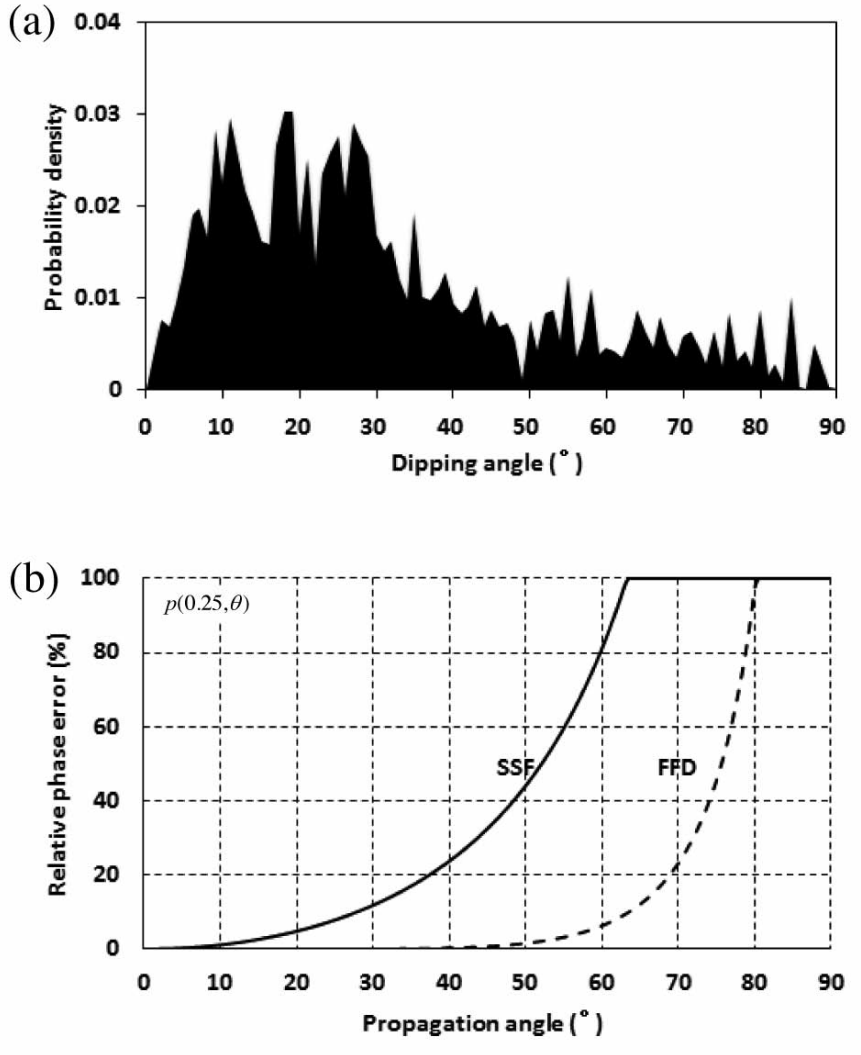

Fig. 7. (a) Angular-heterogeneity spectrum for the geological model in Fig. 6a, (b) Angular spectra of the SSF and FFD migrators with the refractive index n = 0.25.

body and root, the steep subsalt interfaces, the steep subsalt faults, and the horizontal subsalt interface. We expect to characterize these local regions that have a marked deleterious effect on the performance of seismic imaging and need to be handled with more accurate methods. By using recursive migration to split the velocity model into a series of thin slabs for wavefield extrapolation, the velocity and angular complexity coefficients are calculated for each slab. The resulting complexity coefficients of the whole salt model are illustrated in Figs. 8b-8e for both the SSF and FFD migrators.

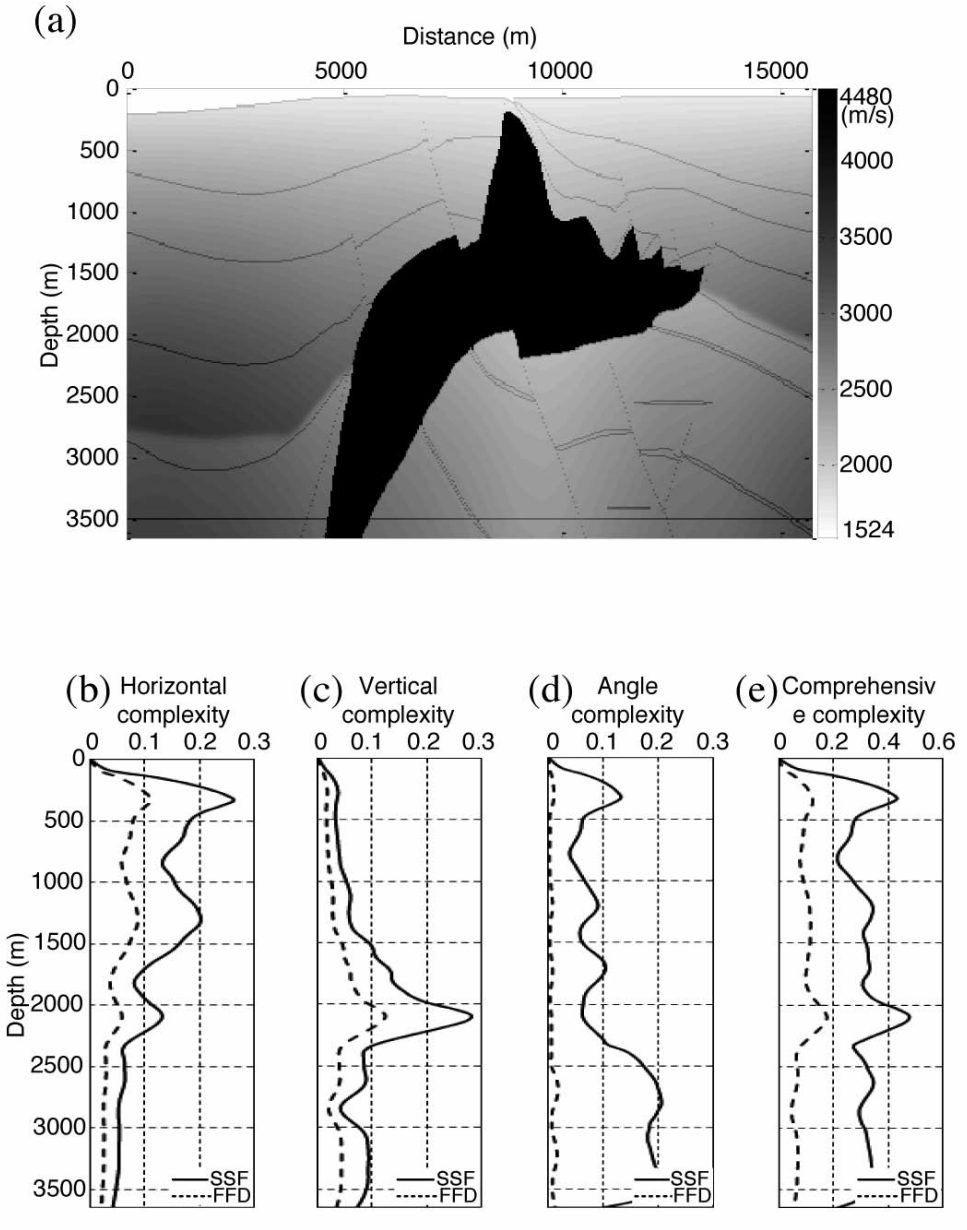

Fig. 8. 2D SEG/EAGE salt model (a) and the corresponding lateral (b), vertical (c), angular (d), and comprehensive (e) complexities.

The lateral velocity complexity appears to peak at a few slabs at 300, 1250, and 2100 m depth, where the velocity contrasts become very strong and cause strong migration noise. The vertical velocity complexity peaks at the bottom of the salt body, with a strong velocity reversion that seriously worsens subsalt imaging. The angular complexity basically reflects the statistical characteristics of dip angles in the model. The steep saltroot and subsalt faults in the subsalt slabs have large angular complexity coefficients that markedly affect interface positioning in seismic imaging. Compared to the upper half of the model, the lower half (below 2000 m) contains more complex structures, resulting in an increase in the comprehensive complexity with increasing depth. The comprehensive complexity curves basically reflect the imaging difficulties of the whole model. The complexity variations between the SSF and FFD migrators illustrate their differences in imaging accuracy, which are demonstrated by the depth migration sections in Fig. 9.

Fig. 10a shows a real velocity model with complex fault blocks, a common geological structure in eastern China. The velocity and angular complexity coefficients for the whole model are calculated and plotted in Figs. 10b-10e for both the SSF and FFD migrators. The lateral complexities are not large for both migrators, indicating gentle to moderate lateral velocity variation. Thus, the time-saving SSF migration appears to be adequate for the accuracy requirement of lateral velocity variations. The vertical velocity complexity curves peak at around 2000 m depth, responding to moderate velocity reversions with a low-velocity belt (Fig. 10a). The angular complexity caused by many steep faults is quite strong for the SSF migration but weak for the FFD migration: this result agrees well with the intuitive estimation of dip-angle distribution for the model. The comprehensive complexity is mainly controlled by the angular complexity components. The comprehensive complexity can be roughly divided into three main sections on the basis of its values. The first section is between 0 and 1500 m: both the SSF and FFD migrators work well in this section because of moderate velocity and angular variation. The second section is between 1500 and 4500 m and contains various complex geological structures. In this section, FFD performs better than SSF. The third section includes the bottom strata, which do not appear to be difficult in terms of seismic imaging, but for which the amplitude fidelity is not guaranteed. The above evaluations of imaging complexity are validated by the SSF and FFD depth migration results, as illustrated in Fig. 11.

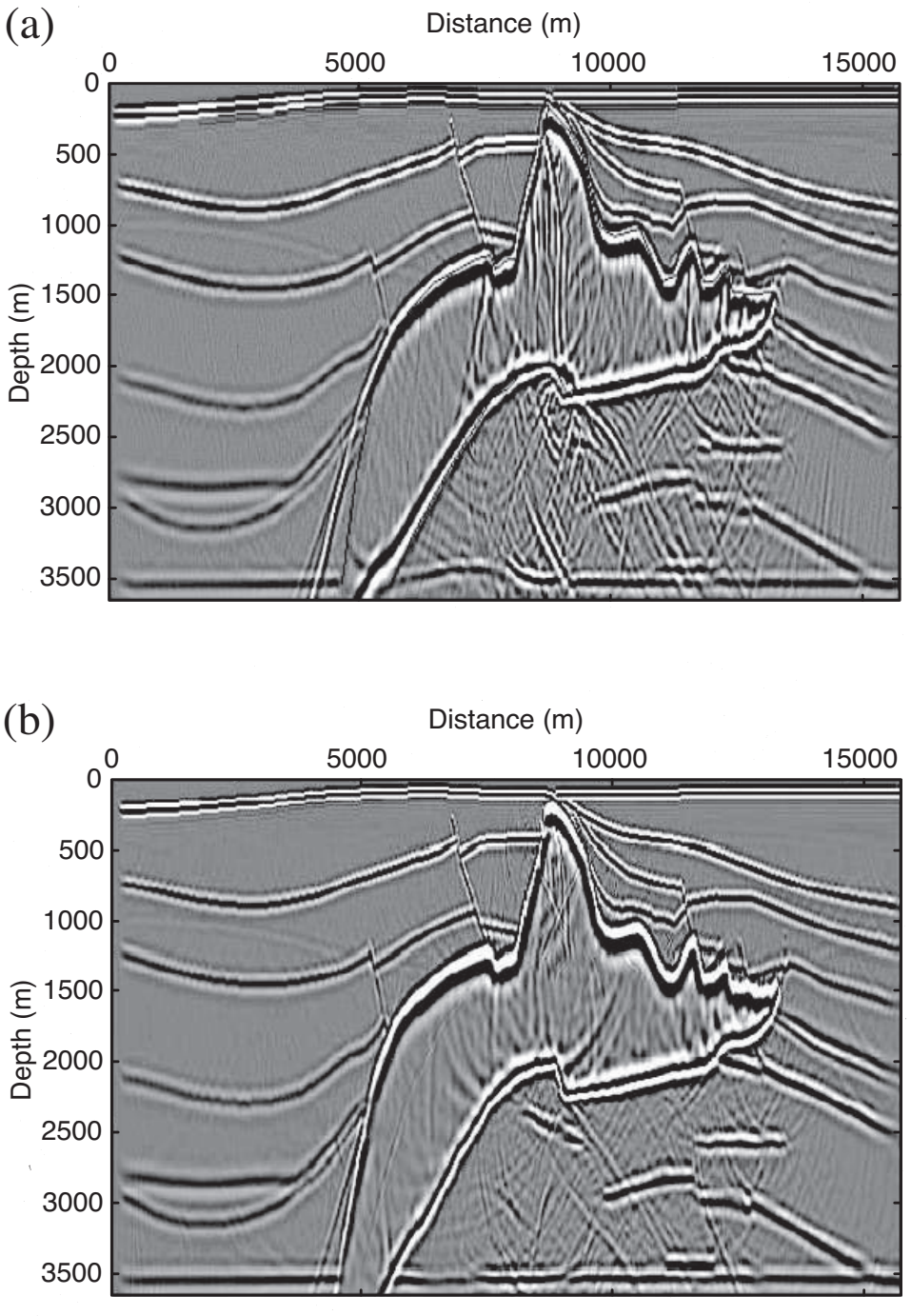

Fig. 9. Poststack depth migration sections of the SEG/EAGE salt model by (a) SSF and (b) FFD.

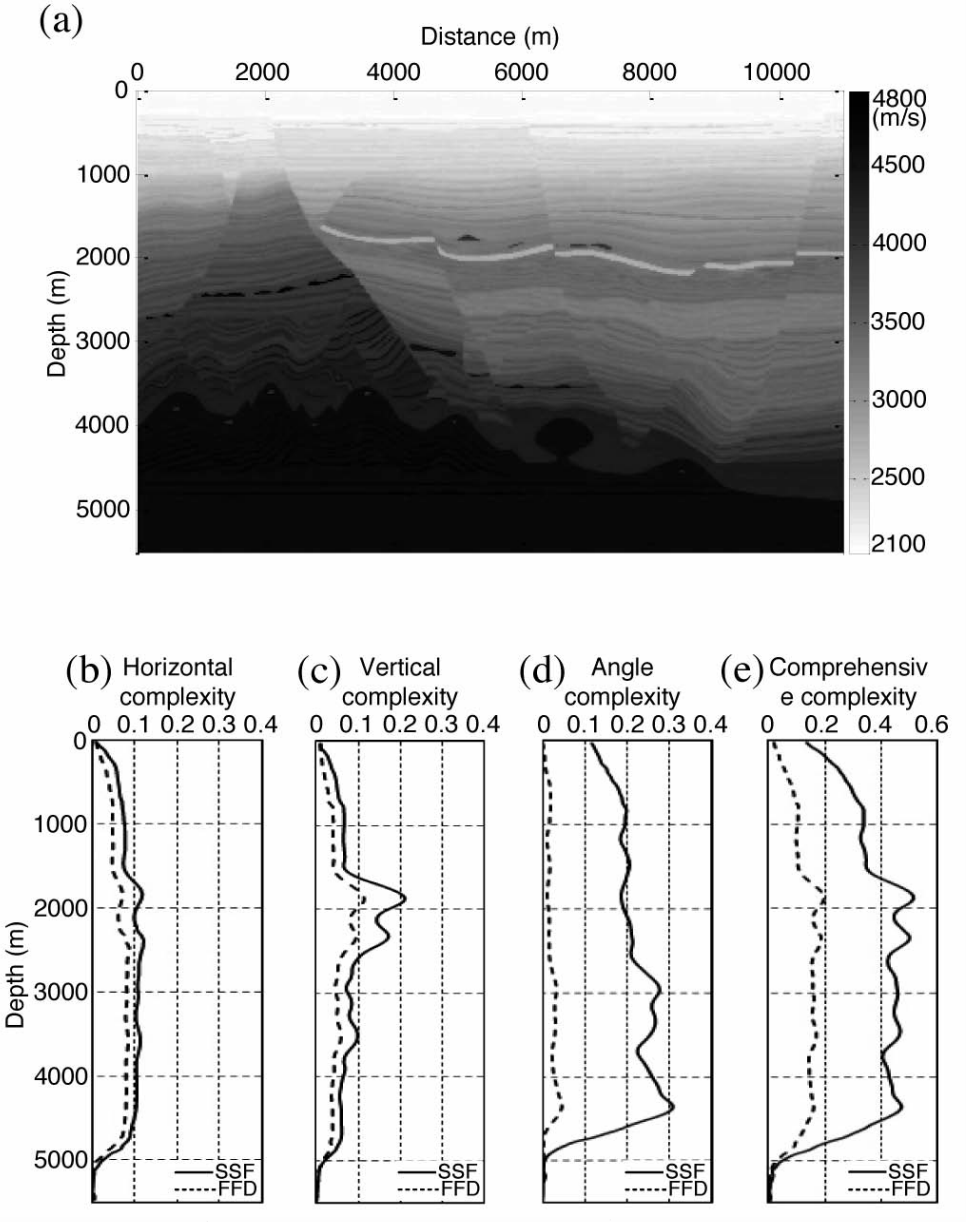

Fig. 10. A velocity model with complex fault blocks (a) and the corresponding lateral (b), vertical (c), angular (d), and comprehensive (e) complexities.

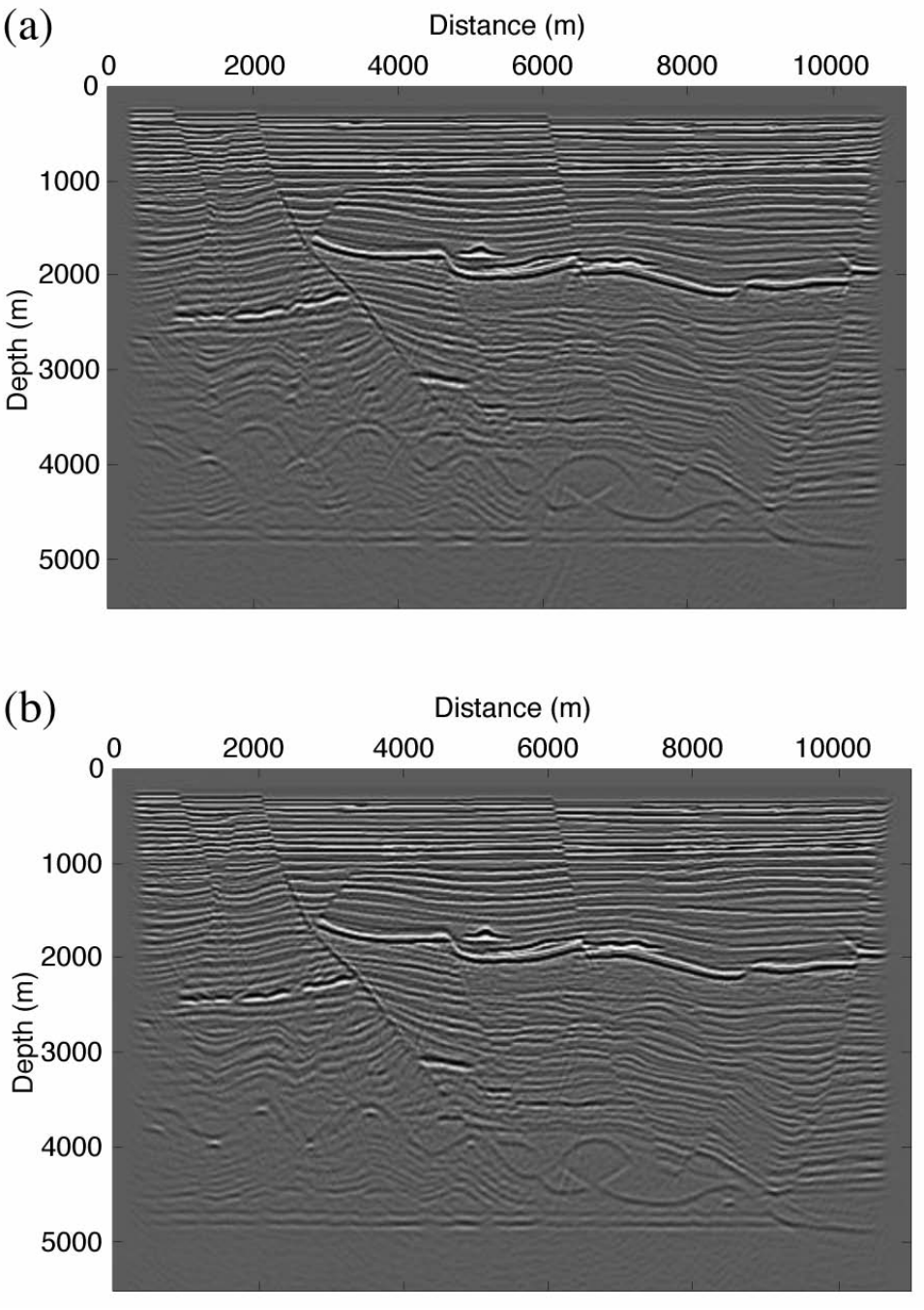

Fig. 11. Poststack depth migration sections of the complex fault model by (a) SSF and (b) FFD.

DISCUSSION and CONCLUSIONS

Quantitative evaluation of the complexity of a velocity model in terms of migrators has been addressed in many previous geophysical studies. The method described herein actually measures the coherent interaction of geological heterogeneity spectra with the utilized imaging operator prior to carrying out migration calculations. Therefore, the method can offer an effective criterion to help choose the most suitable migration method for a given dataset. There are two key factors in the solution to the problem: accurate representation of the velocity variations and dip-angle distribution of a complex model, and scientific definition of complexity coefficients that characterize the correlation between the heterogeneity spectra of the medium and the angular spectra of the migrator. Based on the work of Fu (2010), in this study we tentatively introduce several different methods to achieve this aim, mainly including a velocity co-occurrence matrix for velocity variations and the Hough transform for dip-angle calculations.

We present lateral/vertical VCMs to describe spatial variations in velocity. We optimize the VCMs using d^2 (the square of the vertical distance from an arbitrary position to the leading diagonal) as a scaling coefficient to highlight the large-contrast velocity components that significantly affect seismic imaging. For convenience of analysis, we normalize each VCM by the sum of all its elements to improve its applicability to models of different sizes and varying velocity variations. We directly multiply each element of the VCMs by the corresponding angular error coefficients of a seismic migrator. The resulting MVCMs characterize the illumination feature of a migrator to a heterogeneous slab. We add up all the elements of the MVCMs as the presentation of seismic imaging complexities with respect to lateral/vertical velocity variations. In addition, we use the classical Hough transform to improve the accuracy of edge detection and angle estimation. These methods largely improve the accuracy and applicability of angular-complexity analyses for complex structures with noise-polluted images. Tests on the 2D SEG/EAGE salt model and the classical fault model in eastern China illustrate the applicability and performance of the strategy for complexity analyses in seismic imaging with respect to velocity contrasts and dip-angle variations.

Besides, in our study the complexity at one depth is calculated just for a thin slab around that depth, but not for the whole model or the part of the model above that depth. A measure of the total complexity at a specified depth might be found by integrating all the complexities above the target depth. We believe this type of integration over the whole model could be seen as the ultimate quantitative imaging complexity for the entire model but this remains a question for future research.

By incorporating the heterogeneity spectra of the medium into the angular spectra of the migrator, we tentatively define a complexity coefficient to understand the coherent interference of a migrator with media, and also to evaluate the geological complexity quantitatively in terms of migrators. There has been little research on this issue in previous studies. The strategy used for complexity analyses in seismic imaging is obviously controversial because of the following problems: (1) the heterogeneity spectra of the medium are calculated based on a geological model that does not occur in the real world, and (2) we simply integrate the contributions from velocity contrasts and angular variations, which are actually coupled to each other and thus affect the performance of seismic imaging. In conclusion, a tentative strategy is attempted in this article as a means of opening up the subject for discussion.

ACKNOWLEDGMENTS

The work was supported by The National Natural Science Foundation of China (Grant No. 41130418) and the High Technology Research and Development Program of China (Grant No. 2013AA064202).

REFERENCES

Bourgeois, A., Bourget, M., Lailly, P., Poulet, M., Ricarte, P. and Versteeg, R., 1991. Marmousi model and data. In: Versteeg, R. and Grau, G. (Eds.), Proc. 1990 EAGE Workshop Practical Aspects of Seismic Data Inversion, Copenhagen. EAGE, Houten.

Chopra, S. and Marfurt, K.J., 2005. Seismic attributes - A historical perspective. Geophysics, 70: 3SO-28SO.

de Hoop, M.V., Le Rousseau, J.H. and Wu, R.S., 2000. Generalization of the phase-screen approximation for the scattering of acoustic waves. Wave Motion, 31: 285-296.

Dong, W., Fu, L.Y. and Xiao, Y.J., 2011. Quantitative analysis of the complexity in seismic exploration of the high and steep structures in Kuqa depression. Chin. J. Geophys., 54: 1600-1613 (in Chinese).

Eichkitz, C.G., Schreilechner, M.G., de Groot, P. and Amtmann, J., 2015. Mapping directional variations in seismic character using gray-level co-occurrence matrix-based attributes. Interpretat., 3: T13-T23.

Fu, L.Y. and Duan, Y., 2002. Fourier depth migration methods with application to salt-related complex geological structures. Expanded Abstr., 72nd Ann. Internat. SEG Mtg., Salt Lake City: 895-898.

Fu, L.Y., 2005. Broadband constant-coefficient propagators. Geophys. Prosp., 53: 299-310.

Fu, L.Y., 2006. Comparison of different one-way propagators for wave forward propagation in heterogeneous crustal wave guides. Bull. Seismol. Soc. Am., 96: 1091-1113.

Fu, L.Y, 2010. Quantitative assessment of the complexity of geological structures in terms of seismic propagators. Chin. Earth Sci., 53: 54-63.

Fu, L.Y., Xiao, Y.J. and Sun, W.J., 2013. Seismic imaging studies of complex high and steep structures in the Kuqa depression. Chin. J. Geophys., 56: 1985-2001 (in Chinese).

Gazdag, J., 1978. Wave equation migration with the phase-shift method. Geophysics, 43: 1342-1351.

Guil, N., Villalba, J. and Zapata, E.L., 1995. A fast Hough transform for segment detection. IEEE Transact. Image Process., 11: 1541-1548.

Gao, D., 2003. Volume texture extraction for 3D seismic visualization and interpretation. Geophysics, 68: 1294-1302.

Gao, D., 2007. Application of three-dimensional seismic texture analysis with special reference to deep-marine facies discrimination and interpretation: Offshore Angola, West Africa. AAPG Bull., 91: 1665-1683.

Hough, P.V., 1959. Machine analysis of bubble chamber pictures. Proc. Internat. Conf. High Energy Accelerat. Instrumentat., Geneva: 554-556.

Haralick, R.M., Shanmugam, K. and Dinstein, I., 1973. Textural features for image classification. IEEE Transact. Systems, Man, Cybernetics, 6: 610-621.

Huang, L.-J., Fehler, M.C., Roberts, P.M. and Burch, C.C., 1999a. Extended local Rytov Fourier migration method. Geophysics, 64: 1535-1545.

Huang, L.-J., Fehler, M.C. and Wu, R.-S., 1999b. Extended local Born Fourier migration method. Geophysics, 64: 152-1534.

Le Rousseau, J.H. and de Hoop, M.V., 2001. Modeling and imaging with the scalar generalized-screen algorithms in isotropic media. Geophysics, 66: 1551-1568.

Ristow, D. and Rühl, T., 1994. Fourier finite-difference migration. Geophysics, 59: 1882-1893.

Stoffa, P.L., Fokkema, J.T., de Luna Freire, R.M. and Kessinger, W.P., 1990. Split-step Fourier migration. Geophysics, 55: 410-421.

Wu, R.S., 1996. Synthetic seismogram in heterogeneous media by one-return approximation. Pure Appl. Geophys., 148: 155-173.

Wu, R.S., Jin, S. and Xie, X.B., 1996. Synthetic seismograms in heterogeneous crustal wave guides using screen propagators. Proc. 18th Ann. Seismic Res. Sympos. Monitor. Comprehens. Test Ban Treaty: 290-300.

Yenugu, M., Marfurt, K.J. and Marson, S., 2010. Seismic texture analysis for reservoir prediction and characterization. The Leading Edge, 29: 1116-1121.